metals

MDPI

Article

Effect of Filler Wire on Mechanical Properties, Microstructure and Natural Aging Behavior of 2A55 Al-Li Alloy TIG Welded Joint

Zhihao Liu [1], Pingli Liu [2], Hui Xiang [1], Yang Huang [1], Pengcheng Ma [3], Yonglai Chen [3], Jinfeng Li [1,*] and Ruifeng Zhang [1,*]

[1] School of Materials Science and Engineering, Central South University, Changsha 410083, China
[2] Hebei Lianzhijie Welding Technology Co., Ltd., Changzhou 061000, China
[3] Aerospace Research Institute of Materials and Processing Technology, Beijing 100076, China
* Correspondence: lijinfeng@csu.edu.cn (J.L.); ruifeng.zhang@csu.edu.cn (R.Z.)

Highlights:

What are the main findings?

1. The intergranular Cu-rich phase formed by elemental segregation is not conducive to joint performance.
2. The addition of Ti and Zr in the filler wire effectively refines the grain of the weld and also leads to coarse phases of Ti and Zr in the weld.
3. Natural aging precipitation occurs in welds, and Al3Li particles or GPZs appear in the weld.

What is the implication of the main finding?

The main findings could provide guidance for Al-Li alloy filler wire design and weld aging reinforcement.

Abstract: 2A55 Al-Li alloy is considered to have potential applications in the manufacture of fuel tanks for aerospace vehicles. However, the composition design of filler wires for 2A55 Al-Li alloy TIG welding has not been fully studied. This work focuses on the mechanical properties and microstructure of 2A55 Al-Li alloy TIG welded joints obtained using 2A55 alloy and Al-8Cu filler wire that was designed for this work, as well as the effects brought about by natural aging on them. When filler wire with higher Zr and Ti content was used, the weld grain was significantly refined. Due to the difference in the Cu content of filler wire, the formed Cu-rich phases in welds are significantly different, showing a grid-like distribution in the Al-8Cu weld compared to the dispersed distribution in the 2A55 weld. After welding, the lack of dominant strengthening precipitates caused a sharp softening of the welds. However, Li and Cu atoms dissolved in the Al matrix can precipitate fine and dispersed Al3Li particles and GPZs by natural aging to strengthen the welds. After natural aging, the yield strength (YS) of the 2A55 joint increased by 24.1% compared with the 14.7% improvement of the Al-8Cu joint.

Keywords: 2A55 Al-Li alloy; manual TIG welding; natural aging of weld; grain refinement

Citation: Liu, Z.; Liu, P.; Xiang, H.; Huang, Y.; Ma, P.; Chen, Y.; Li, J.; Zhang, R. Effect of Filler Wire on Mechanical Properties, Microstructure and Natural Aging Behavior of 2A55 Al-Li Alloy TIG Welded Joint. *Metals* **2023**, *13*, 347. https://doi.org/10.3390/met13020347

Academic Editor: Xudong Qian

Received: 31 December 2022
Revised: 5 February 2023
Accepted: 6 February 2023
Published: 9 February 2023

1. Introduction

Due to their high specific strength, low density, and high elastic modulus, Al-Li alloys are considered to have great advantages in the aerospace field and are admissible substitutes for traditional Al-Cu-based alloys [1,2]. Each 1% lithium added will reduce the density of the aluminum alloy by about 3% and increase the elastic modulus by about 6%, which can greatly improve the carrying capacity of the aerospace vehicle [3]. As a typical third-generation Al-Li alloy, 2A55 alloy is micro-alloyed with Mg, Ag, and Zn to control the precipitation of the alloy during the heat treatment for high strength while ensuring other performances such as low anisotropy and high fatigue resistance [4–7].

The connection technology is essential to ensure parts integrity and improve service safety during service. Growing attention has been paid to the welding approach of Al-Li alloys due to fewer restrictions on the component shape compared with mechanical connection [8]. Among various welding techniques, TIG welding is extensively used in the repair welding of aerospace vehicle fuel tanks due to its flexible operation, low cost, and high applicability [9,10]. However, studies have shown that when TIG welding is used for aluminum alloy welding, the joint has defects such as pores and micro-cracks [11–14]. Furthermore, the strength and plasticity of the joints are also greatly reduced due to the severe segregation and the lack of strengthening precipitates after welding resulting from the non-equilibrium solidification process in the melt pool region [15–18].

As a weak area, the poor performance of TIG welded joints will compromise safety. There are some ways to strengthen the welds based on obtaining a good quality joint. The welding process is composed of melting and rapid solidification; thus, the obtained weld structure can be regarded as the as-cast structure. Therefore, adding an appropriate amount of modifier such as Zr to the filler wire is conducive to the formation of coherent Al_3Zr particles during the solidification process. Coherent particles can provide nucleation sites to increase the nucleation rate during solidification. This results in a strong non-uniform nucleation effect resulting in fine weld grains that enhance the weld's strength and toughness [8,19]. As another commonly used modifier, Ti also has a similar effect to Zr during molten metal solidification. In addition, when Ti is added alone or in combination with Sr, the weld performance can be improved by modifying the microstructure of welds [20,21].

Although trace addition of modifiers can improve the weld performance by refining grains or changing the weld's microstructure during solidification, problems such as segregation and lack of strengthening precipitates in the welds are still problems. To further improve the weld performance, some post-treatment, such as rolling, shot peening, and heat treatment, can be considered [22,23]. Mechanical post-treatment is generally used to modify the surface of the joint [24]. Post-weld heat treatment can release the residual stress of the joint more comprehensively or modify the microstructure of the joint to improve joint performance. When the 2219 alloy variable polarity TIG welded joint was subjected to a series of heat treatments, including solution treatment (535 °C, 30 min), water quenching, and artificial aging (175 °C, 12 h), the yield strength (YS), tensile strength (UTS) and elongation (EL) of the joint increased by 42.6%, 43.1%, and 18.4%, respectively. Additionally, the joint hardness value reaches 98% of the base metal (BM) [9]. After artificial aging of laser pressure welded joints of 2198 Al-Li alloy, it was found that T_1 precipitates appeared in the area where the strengthening precipitates should be absent, which contributed to the joint performance improvement [25]. It is foreseeable that for heat-treatable-strengthened aluminum alloys, post-weld heat treatment is beneficial for strengthening the joint. Affected by the shape of the weldment, artificial aging cannot be performed on welds in many scenarios. At this time, the natural aging of the welds of the age-hardening Al-Cu-Li alloy can be considered [26–33]. After long-term (11 years) natural aging at ambient temperature, AA2219-T87 TIG welded joints showed a 35% and 20% improvement in YS and UTS, respectively [34]. Relatively short aging time also has a certain effect on improving the performance of joints. After 150 days of natural aging, the UTS of 7075 alloy welded joints with Al-Zn-Mg-Cu-Ti/TiB_2 alloy filler wire increased from 300 MPa to 328 MPa [35]. Therefore, natural aging can be considered for scenarios where artificial aging is not well applied. However, the effect of filler wire composition on the natural aging precipitation of TIG welded joints of 2A55Al-Li alloy remains to be explored.

In this work, Al-8Cu filler wire that was designed for this work and 2A55 Al-Li alloy filler wire were used for manual TIG welding of 2A55 Al-Li alloy. The effects of filler wire composition on the mechanical properties, microstructure, and precipitation evolution of the joints were clarified and exploited. The types and quantities of natural aging precipitates and their effects on joint performance were further investigated. This work could provide guidance for Al-Li alloy filler wire design and weld aging reinforcement.

2. Materials and Methods

2.1. Materials

In this study, 80 mm (rolling direction) × 200 mm × 2 mm (thickness) T6-aged 2A55 Al-Li alloy was used as the BM. The T6-aged is a solid solution at 520 °C for 1 h, followed by water quenching, then aged at 175 °C for 20 h. In addition, to use 2A55 alloy as the filler wire, an Al-8Cu filler wire was designed and fabricated in this study. Cold-rolled 2A55 alloy with a thickness of 2 mm and self-cast Al-8Cu alloy ingot was cold rolled to 1.5 mm and then processed into 1.5 mm × 1.5 mm × 500 mm strips by wire cutting. Table 1 shows the composition of the BM and filler wire.

Table 1. Measured composition of BM and design composition of filler wire.

Material	Cu	Li	Ag	Mg	Zr	Ti	Zn	Mn	Be	Al
2A55	3.81	1.28	0.41	0.43	0.11	0.06	0.39	0.28	/	Bal.
Al-8Cu	8.00	/	/	/	0.30	0.30	/	/	0.0005	Bal.

2.2. TIG Welding Process

The filler wire was desmuted before the welding process, and the filler was first soaked in 10 wt.% NaOH solution for 10 min, rinsed with distilled water, and then immersed in 30 wt.% HNO_3 solution for 5 min. As for the BM, the surface layer is removed with sandpaper before welding, and the debris is removed ultrasonically. After drying, all materials were vacuum-packed for further testing.

The grain morphology of the welding BM is shown in Figure 1. The grains are still deformed after heat treatment. In this study, rolling-oriented butt welding is selected. Manual TIG welding experiments with manual wire feeding were carried out in Jiangsu LianJie Welding Technology Co., Ltd., using a WSME-315 welding machine. In the welding process, high-purity argon gas was used as the protective atmosphere. The welding parameters are listed in Table 2.

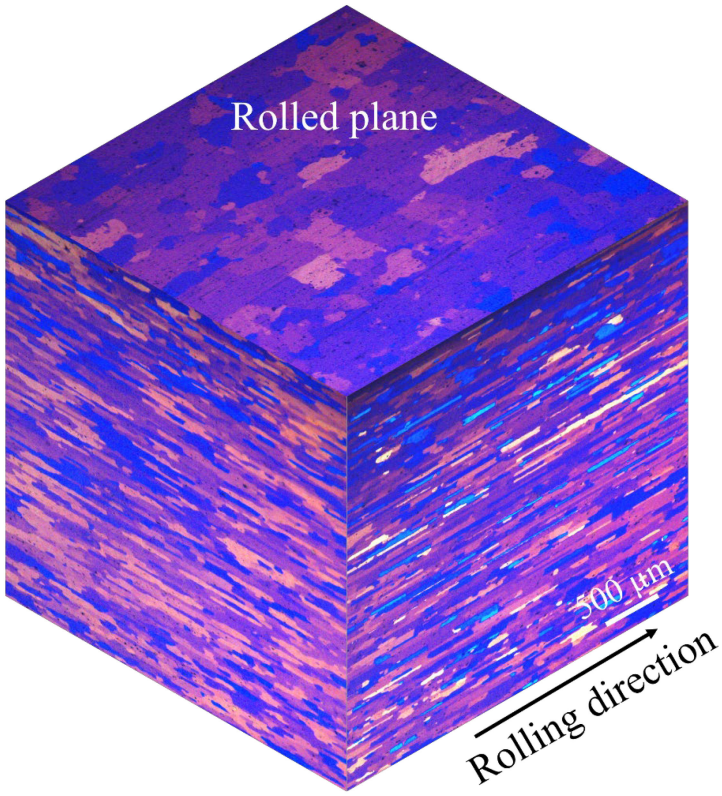

Figure 1. Three-dimensional metallography of T6-aged 2A55 Al-Li alloy.

Table 2. Welding parameters.

Parameters	Base Current (A)	Voltage (V)	Speed (mm/min)	Argon Flow (L/min)
Value	80	20	100	9

2.3. Mechanical Properties

The tensile test was performed on the MTS-810 testing machine at a rate of 2 mm/min. The original length for elongation measuring was in the specimen center set as 25 mm. The tensile test samples were processed by wire cutting according to the standard GB/T 228.1-2010. Before the tensile test, samples were ground on 80-grit sandpaper to remove the excess weld metal. The Vickers microhardness test is carried out according to the standard GB/T 27552-2011, and the middle of the weld cross-section is selected. The point spacing was 0.5 mm for 10 s under a load of 4.9 N. In particular, the spacing was 0.2 mm near the fusion line to obtain the microhardness of the fine equiaxed grains.

2.4. Microstructure Characterization

Optical metallographic specimens polished with diamond slurries were corroded by Keller reagent for 10 s and then characterized by Leica optical microscope. Scanning electron microscope (SEM) images were taken at 25 kV using a Sirion 200 Field Emission Scanning Electron Microscope with backscattering (BSE) mode and X-ray energy dispersive spectrum (EDS) capability to characterize the joint's microstructure and elemental distribution. Types of precipitates in the sample are characterized by FEI Tecnai G2 20 transmission electron microscopy (TEM) and Talos F200X scanning transmission electron microscopy (STEM). The samples were ground to 60–80 μm on 2000-grit sandpaper and then prepared by twin-jet electropolishing in a mixed solution of nitric acid and methanol (volume ratio 1:3). The working temperature and the currents were −30 °C and 90 mA, respectively.

3. Results

3.1. Microstructure of Joints

Optical micrographs of joint cross-sections obtained by manual TIG welding are shown in Figure 2a,d. According to the grain morphology, the joint is divided into several zones, including heat affected zone (HAZ), fine equiaxed zone (FEQZ), columnar zone (CZ), and equiaxed dendrite zone (EQDZ). Compared with the grain shape of the BM, the grains in the HAZ far from the fusion line still maintain the rolled grain shape. As shown in Figure 2b,e, the grain shape closer to the fusion line has changed due to the influence of heat input, and there is a tendency for grain coarsening and even partial melting occurs.

It is the non-uniform nucleation that leads to the formation of a large number of grain nuclei at the edge of the melt. At this time, the heat dissipation rate is fast, and the cooling rate is large, leading to fine equiaxed grains forming and avoiding dendrites formation. The width of the FEQZ is approximately 50 μm, as measured by the markers in Figure 2b,e, and a gradual narrowing characterizes it from the lower part to the upper part of the welds. Because during the welding process, the temperature of the upper part is higher due to constant heat input, and there is a melt flow, causing the FEQZ formed in the upper layer to remelt. The consequence is that only a thin layer of fine equiaxed grains is formed in the upper part. Due to a strong heat dissipation directionality, columnar grains form in the welds near the FEQZ and have a larger tendency at the bottom of the weld. Finally, with the progress of solidification and the growth of columnar grains, the heat dissipation rate becomes slower, and the melt is almost isothermal. When the overall temperature decreases to a critical value, grain nuclei appear everywhere in the melt. At this time, the temperature gradient (G) level in the center of the weld nugget is low, and the growth rate (R) of the grain in the center of the weld nugget is faster. When the value of G/R is small, the tendency of constitutive supercooling is large, and the heat dissipation has no directionality at this time, as shown in Figure 2c,f. The result is that the grains formed in the center of the welds are equiaxed dendrites. The statistical results of the grain size of the

weld nugget area in Figure 2c,f show that the average equivalent grain diameter of the weld using Al-8Cu filler wire is 110 μm while using 2A55 filler wire is 254 μm, which implies that 0.3 wt.% Ti and Zr in Al-8Cu filler wire, compared with 0.11 wt.% Zr + 0.06 wt.% Ti in 2A55 filler wire has a better effect on refining weld grains.

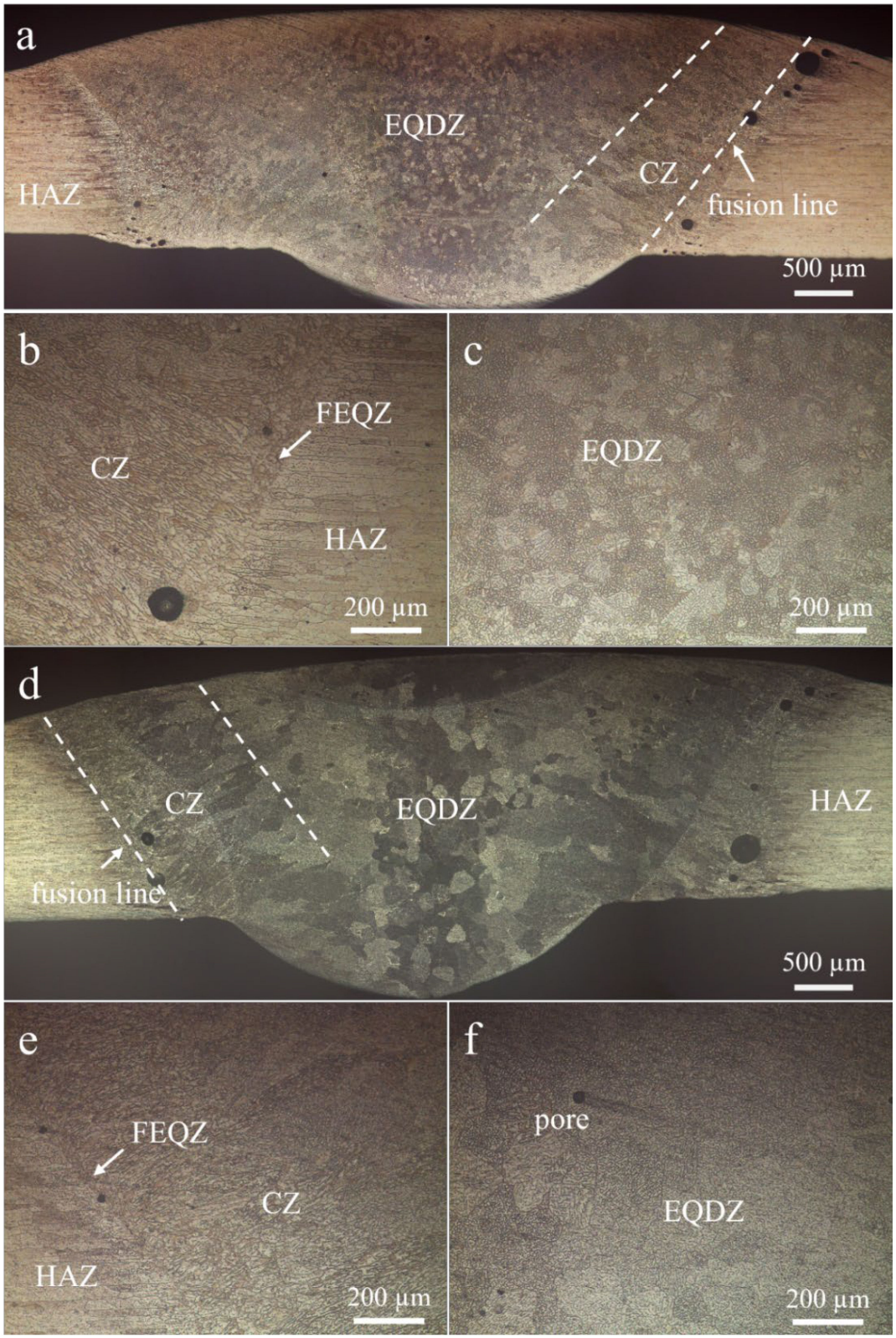

Figure 2. Overall metallographic images of the cross-section of the (**a**) Al-8Cu joint, (**d**) 2A55 joint, and magnified metallographic image of a typical area of the (**b**,**c**) Al-8Cu, (**e**,**f**) 2A55 joint.

The SEM images in the backscattering mode of welds are shown in Figure 3. There are a large number of Cu-rich phases in welds, and the morphology of phases in the intragranular and interface is different. The interface is occupied by long strips of Cu-rich phases, while the phases within the grains are point-like. The data recorded in Table 3 are the EDS analysis results of various phases in the weld, indicating that the phase existing in the weld is almost all Cu-rich phase. Due to the significant difference in the Cu content in the welds, the content, morphology, and distribution of the Cu-rich phase in the two welds are also different. The area fractions of the Cu-rich phase in Al-8Cu weld and 2A55 weld are 6.8% and 4.4%, respectively. An obvious result is that, as shown in Figure 3b,d, the interfacial Cu-rich phases in the EQDZ in the Al-8Cu weld are roughly reticulated, while the interfacial phases in the 2A55 weld are extremely discontinuous. In addition, the Cu content of the interfacial Cu-rich phase is almost twice that of the intragranular phase because of the rapid solidification of Al-Cu alloys. In general, Cu has a significant tendency to aggregate at the grain boundaries during the solidification process. The aggregation of Cu elements at grain boundaries or within the grain causes inhomogeneity of the entire grain composition, namely element segregation. Figure 4a,b shows the EDS mapping results of the two welds, indicating that Ti and Zr segregation is also present in the weld. As a possible segregation element, Mg did not show segregation in this work. Additionally, as marked in Figure 3a, a new phase with an equivalent diameter of about 10 μm appeared in the welding seam of Al-8Cu filler wire, which was determined to be Ti and Zr phases by EDS analysis. Moreover, the porosity of the joint was calculated to be 3% for the Al-8Cu joint, compared to 5% for the 2A55 joint. In addition, the voids are concentrated on the fusion line. Since the solidification near the fusion line is a rapid cooling process, the rapid solidification of molten metal forms fine equiaxed grains, which also hinders the escape of gas generated by welding and produces a large number of pores.

3.2. Mechanical Properties

3.2.1. Microhardness Distribution of Joints

The microhardness curves in the weld of the two joints one week and six months after welding are shown in Figure 5a. The microhardness of the BM is indicated by the dotted line in the figure, which is 187.4 HV. As depicted in Figure 5b, the average microhardness of the Al-8Cu weld is 88.46 HV for one week after welding, and that of the 2A55 joint is 87.46 HV. However, when the natural aging time comes to six months, the average microhardness increases to 95.70 HV and 98.21 HV, respectively. It can be seen that after TIG welding, joints are severely softened, and the weakest parts are in the weld nugget area. Although the microhardness of the joints increases to a certain extent after natural aging, it is still much lower than that of the BM.

3.2.2. Tensile Properties of Joints

The engineering stress-strain curves and YS, UTS, and EL of the two joints are given in Figure 6a,b, respectively. As shown in Figure 6, when the joint has completed six months of natural aging, the YS increase of the 2A55 joint is greater than that of the Al-8Cu joint. The YS of Al-8Cu and 2A55 joints increased by about 14.1% and 24.7%, respectively. Similar to the joint microhardness test results, joint performance improved after natural aging. However, although the YS of the joints increased with aging time, it was still much lower than that of the BM of 527.7 MPa. In addition, the EL of the best tensile specimen is about 20.7% of the BM. Additionally, the deformation basically occurs in the welds.

3.3. Precipitation Behavior of Welds

Previous tensile and microhardness tests showed poor performance of the 2A55 Al-Li alloy TIG weld joints. However, after a period of time, there was a different degree of improvement in the performance of the two joints. This is expected to be the melting and re-precipitation of the strengthening precipitates in the welds.

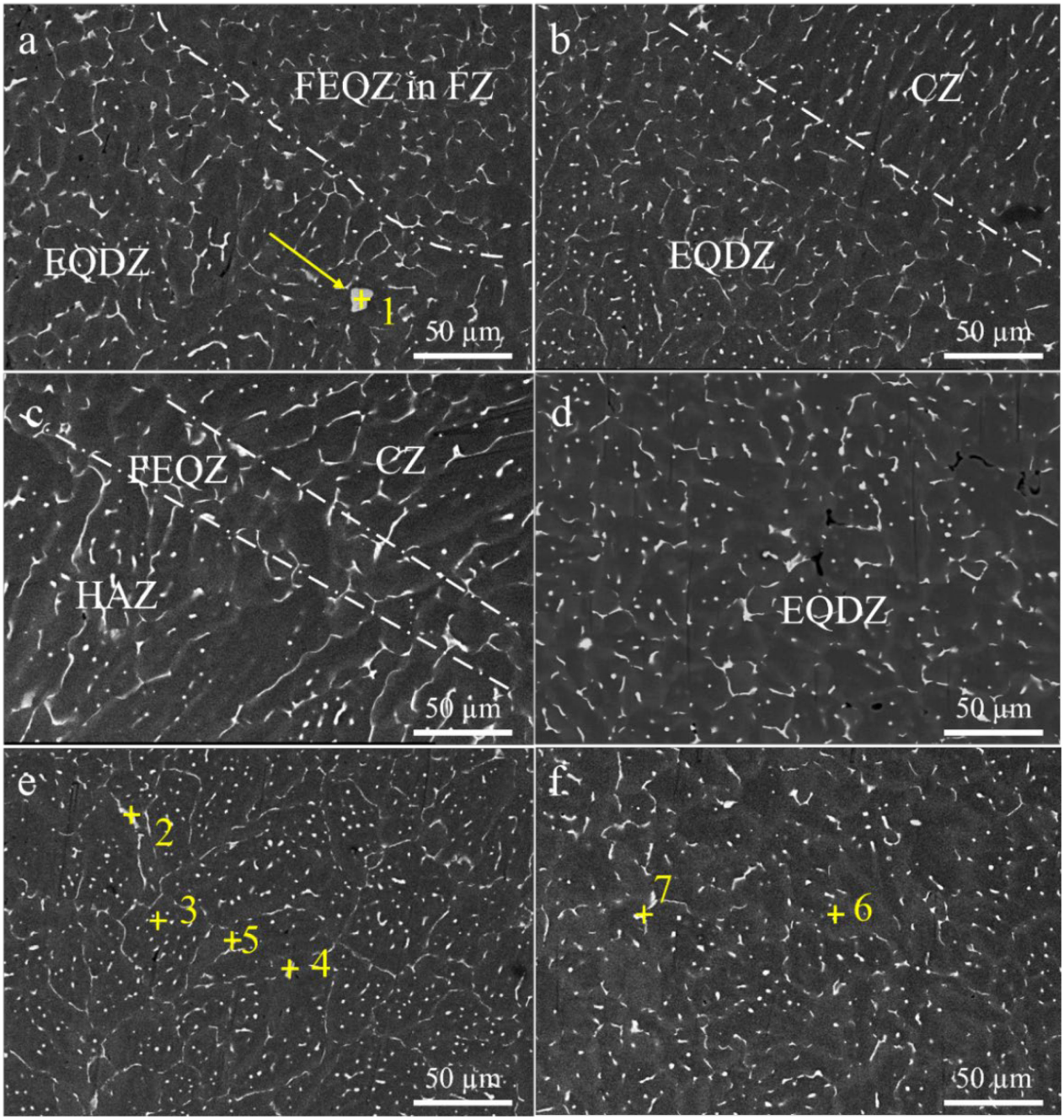

Figure 3. SEM image in BSE mode of (**a**) fusion zone (FZ), (**b**) rear end of columnar grain in Al-8Cu weld and (**c**) fusion line, (**d**) FZ in 2A55 weld and the location of the EDS analysis points for the different morphological coarse phases in the EQDZ of (**e**) Al-8Cu, (**f**) 2A55 weld.

Table 3. The EDS analysis results of the corresponding point in Figure 3 (wt.%).

	1	**2**	**3**	**4**	**5**	**6**	**7**
Cu	/	23.81	13.30	/	26.17	12.68	19.85
Zr	14.17	/	/	8.37	/	/	/
Ti	26.93	/	/	19.22	/	/	/
Al	Bal.	Bal.	Bal.	Bal.	Bal.	Bal.	Bal.

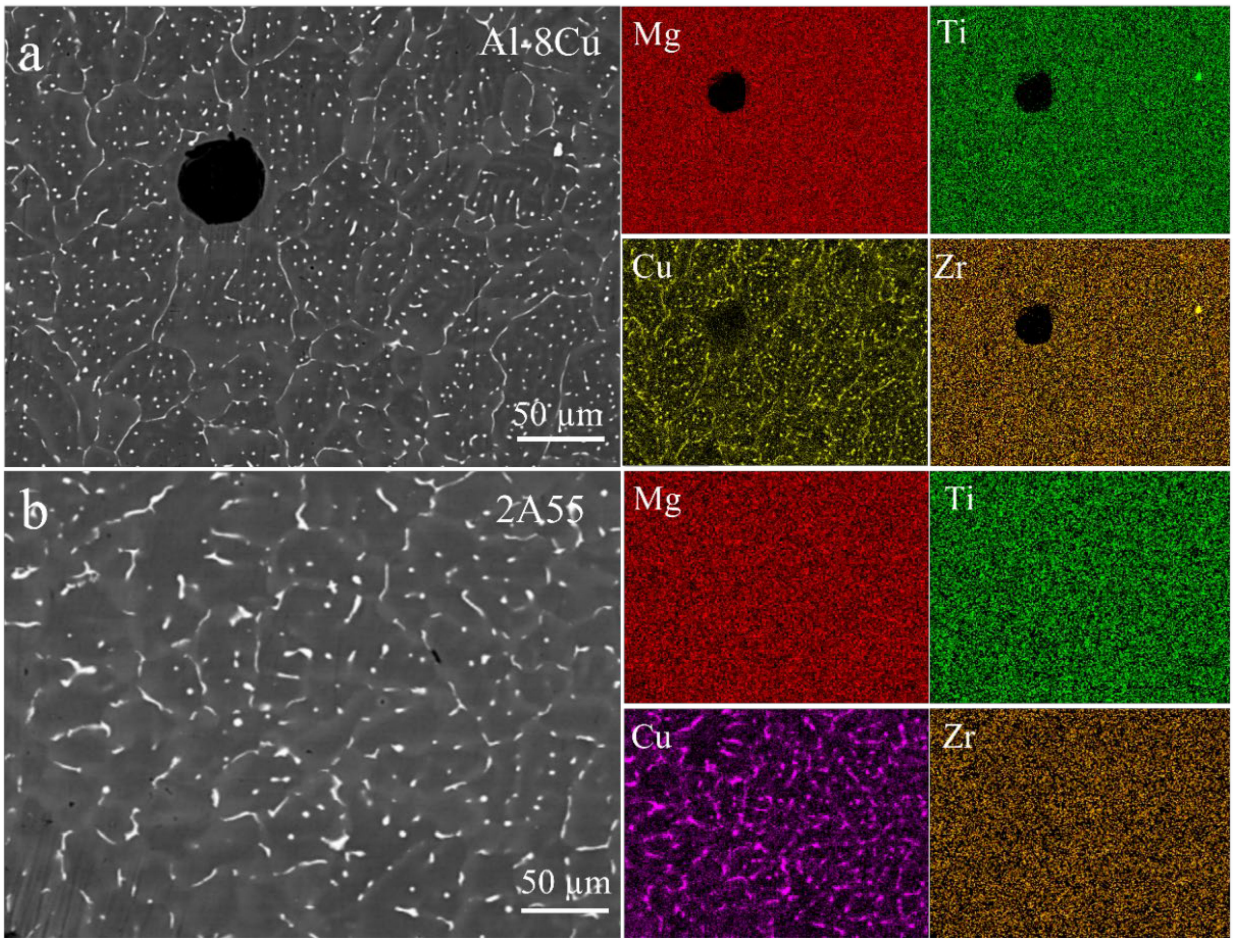

Figure 4. (**a**) Al-8Cu, (**b**) 2A55 weld EDS mapping analysis area and the distribution of Mg, Cu, Ti, and Zr.

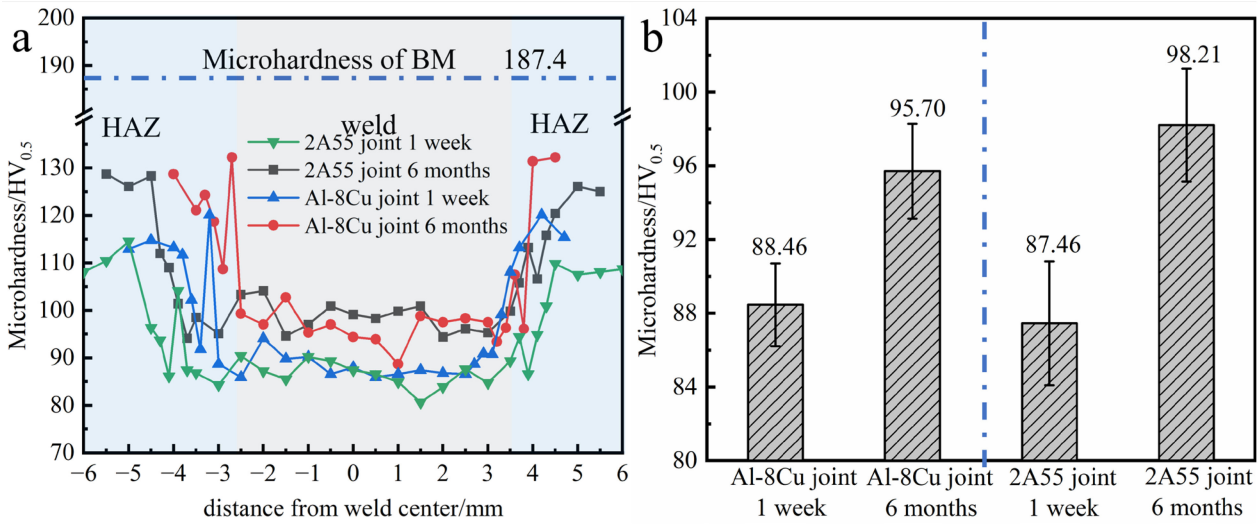

Figure 5. (**a**) Vickers microhardness distribution curve of the joints, (**b**) the average microhardness of the welds before and after natural aging.

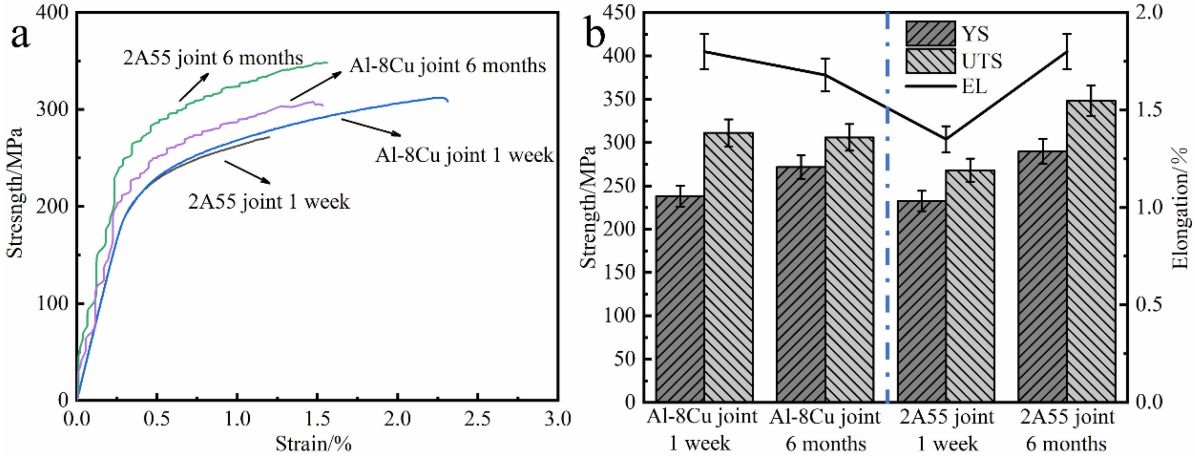

Figure 6. (**a**) The engineering stress-strain curves of the Al-8Cu joint and 2A55 joint one week and six months after welding and (**b**) the YS, UTS, and measured EL (with 5% human personal error) in the tensile test.

To characterize the precipitation in the welds, the weld of the two joints one week and six months after welding was subjected to differential scanning calorimetry (DSC) test. The DSC test results in Figure 7 show two endothermic (peak A and peak C) heating effects when the welds are continuously heated. Related studies have proved peak A represents the melting endothermic peak of Al_3Li + GPZ, while peak C is the melting endothermic peak of Al_3Li remaining in the sample or precipitated during the DSC test. In addition, there are several exothermic heating effects where peaks B and E represent the precipitation of Al_3Li and Al_2Cu, respectively [8,36,37].

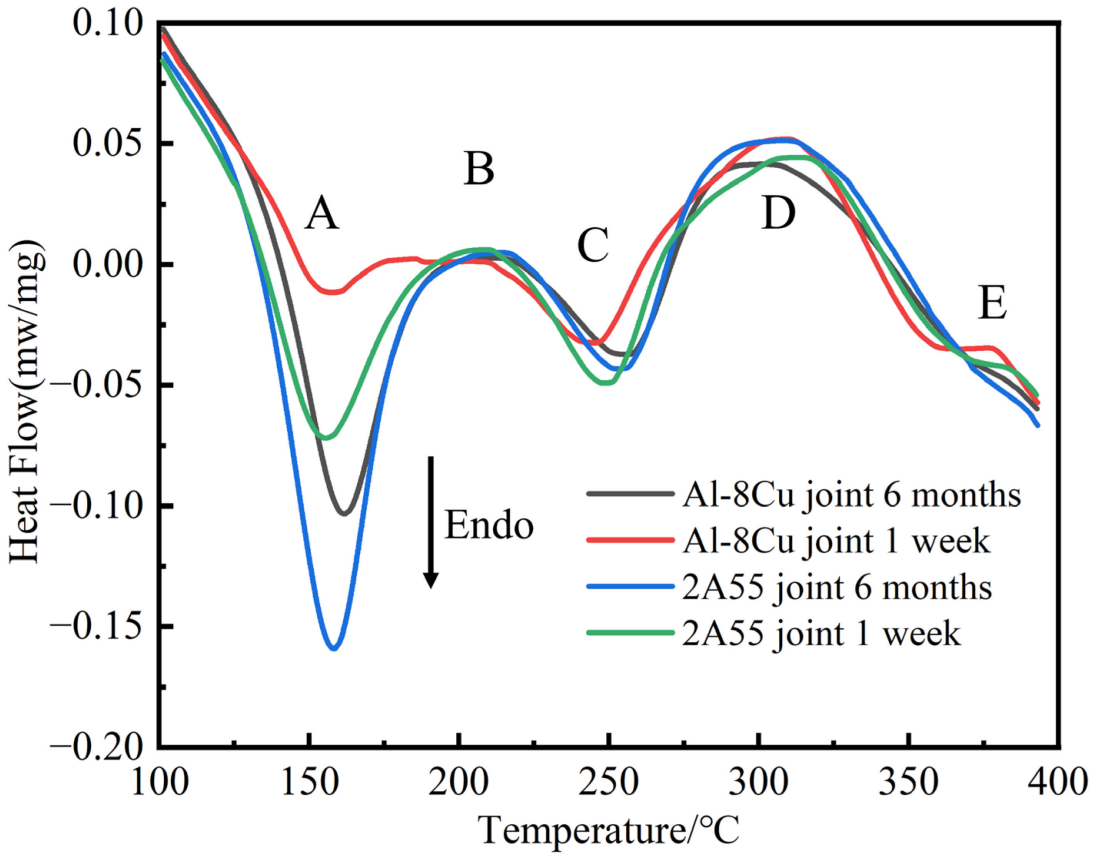

Figure 7. DSC curves of Al-8Cu and 2A55 welds with different aging times.

To further characterize the source of reinforcement and the differences in the precipitation behavior between the two welds, TEM analysis was performed. When the Al-8Cu joint (Figure 8a,c) was placed from one week to six months, the corresponding δ′(Al_3Li) + β′(Al_3Zr) + θ′(Al_2Cu) diffraction patterns did not change significantly, while the 2A55 joint (Figure 8b,d) has a very distinguished change. However, the diffraction pattern in Figure 8c shows the presence of GPZ within the Al-8Cu weld after natural aging. The TEM dark field image of the 2A55 weld is shown in Figure 8d, indicating that the differences in the previous diffraction patterns are mainly caused by the precipitation of Al_3Li. Additionally, it can be noted from Figure 8d that after natural aging, no Cu-containing precipitates appear in the 2A55 weld. High-magnification TEM images of the two welds are shown in Figure 9. As depicted in Figure 9a,b, the main precipitate in the Al-8Cu weld is GPZ, while the 2A55 weld has a large number of dispersed Al_3Li particles and few GPZs with smaller sizes. Furthermore, as shown in Figure 9c,d, particles of approximately 20 nm in size appear in both welds and are identified as Ag-rich phases by EDS mapping testing.

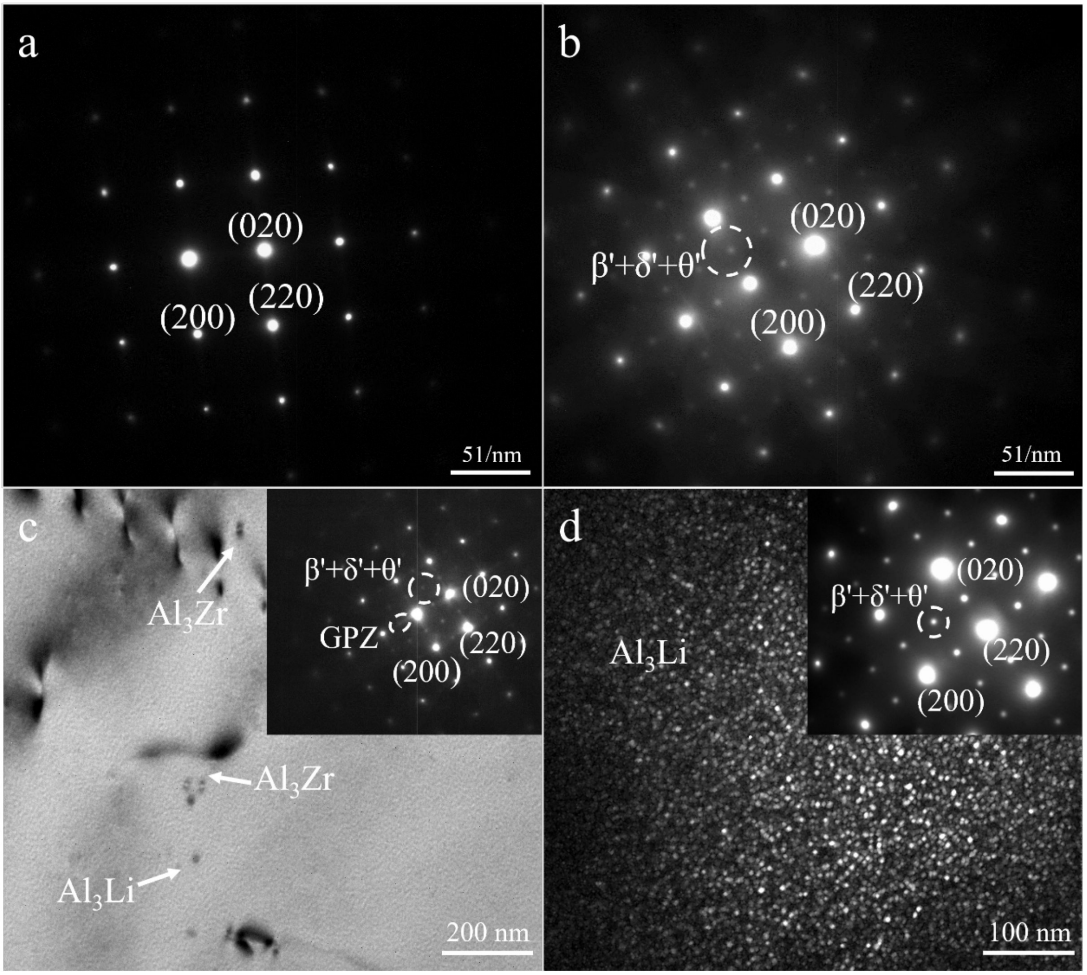

Figure 8. Diffraction pattern of (**a**) Al-8Cu weld, (**b**) 2A55 weld after one week of natural aging under <100> matrix zone axis, and (**c**) TEM bright field image of Al-8Cu weld after six months of natural aging, and (**d**) TEM dark image of 2A55 weld after six months of natural aging under <100> matrix zone axis.

According to the results of the DSC test and TEM characterization, it was determined that a large number of GPZs appeared in the Al-8Cu weld during natural aging, while the 2A55 weld mainly precipitated fine and dispersed Al_3Li.

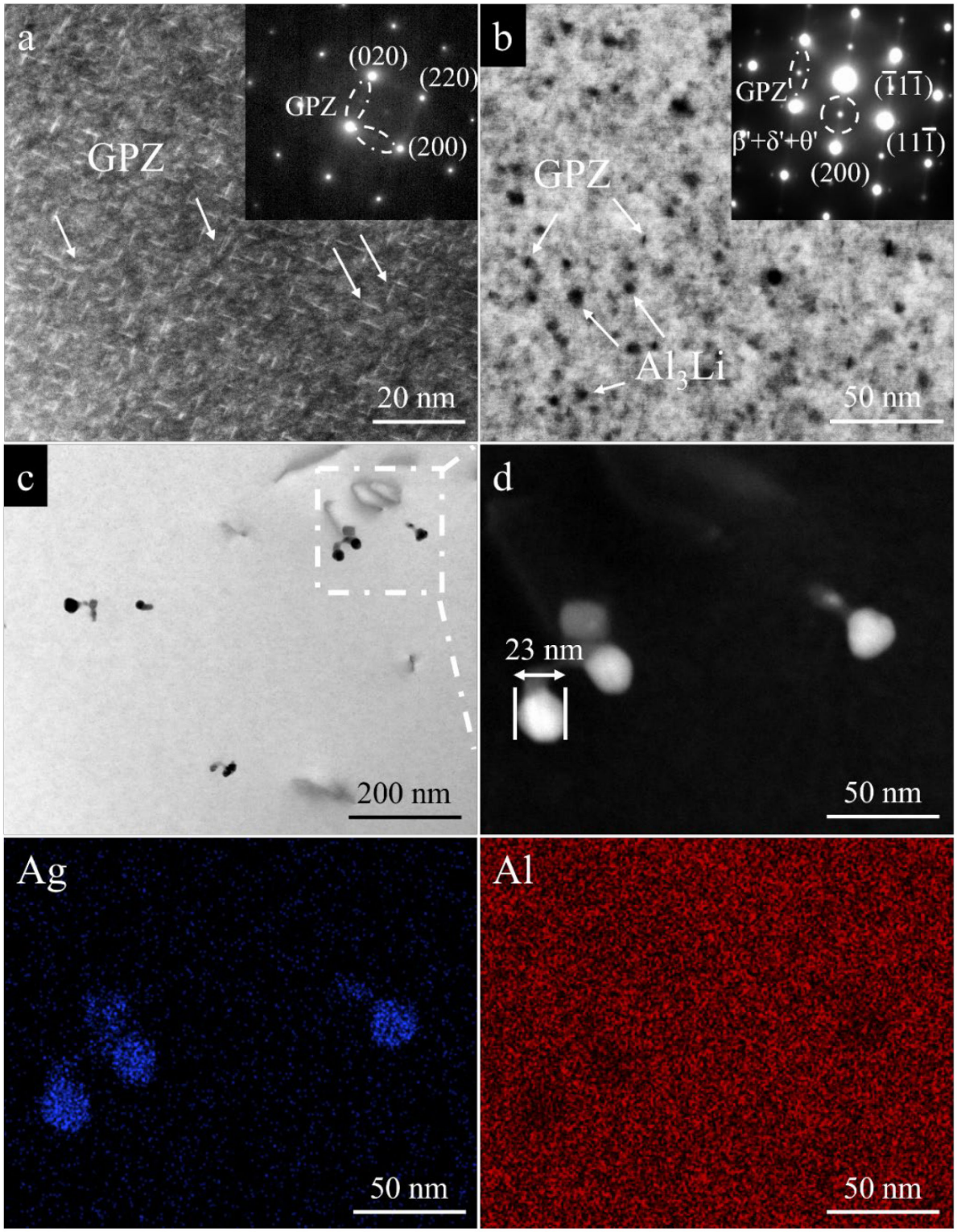

Figure 9. (**a**) High angle annular dark field (HAADF) of Al-8Cu weld after six months of natural aging under <100> matrix zone axis, (**b**) TEM bright field image of 2A55 weld after six months of natural aging under <110> matrix zone axis, (**c**) TEM bright field image and (**d**) EDS mapping analysis area of Ag-rich phase present in two welds.

4. Discussion

4.1. Effect of Filler Wire on Microstructure

The purpose of the filler wire composition design is to reduce the hot tearing tendency of the joint during solidification and improve joint performance. As depicted in Figure 2a,d, when the Al-8Cu filler wire and 2A55 filler wire designed in this study were used in manual TIG welding experiments, well-formed joints were obtained, and no obvious hot cracking was found. There are some large pores at the fusion line, which deteriorates the tensile properties of the joints. The samples fractured prematurely during the tensile process and showed poor joint EL. In the process of rapid solidification, the low-melting-point substances were squeezed to the grain boundary to form a liquid film, and hot tearing was generated under the action of solidification stress in the final stage of solidification [35]. In addition, during the solidification process, a large number of dendrites are formed due to the influence of constitutive supercooling. There are gaps between the dendrite arms due to the characteristics of dendrite growth [38,39]. If the molten metal is not filled and healed in time, hot cracks will also occur. One way to reduce hot tearing tendency is to narrow the solidification interval; studies showed that a wider solidification range would require longer passages for liquid metals capable of healing dendritic gaps [35,40,41]. Both the Al-8Cu filler wire and 2A55 filler wire designed in this work have a large solidification range. Even under non-equilibrium solidification conditions, the 2A55 weld with 3.8-Cu wt.% composition has a wider solidification range than the Al-8Cu weld due to the left shift of the solidus line. For Al-8Cu weld, many Al-Cu eutectic can be produced in the Al-8Cu weld, which has good fluidity and can play a healing effect in time. In addition, during the final solidification period, the grains are almost surrounded by remaining molten metal [42]. A large number of fusible substances at the grain boundary are easy to flow between the grains or dendrites, thus playing a filling or healing role. The solidification stress at this time does not pose the threat of forming hot cracking. Finally, the fusible substances solidify and form the lattice-like grain boundary Cu-rich phases, as shown in Figure 3a,b. For 2A55 weld, due to the lower Cu content, even under the influence of non-equilibrium solidification, there are only a small number of low-melting eutectics crowded at the grain boundaries. At the end of solidification, a small amount of molten metal also corresponds to very little closed liquid film, and the solidification cracking sensitivity is not high at this time [43]. However, the dendrite gaps can still be filled during the dendrite growth period, and a joint without obvious solidification cracking was obtained, as shown in Figure 2d.

However, the solidification of fusible materials at grain boundaries will cause element segregation. The element segregation phenomenon will cause uneven deformation of the joint during the tensile test and greatly reduce the ductility of joints [11–13]. As depicted in Figure 3, a large number of dendrites and intergranular Cu-rich phases were present in the welds. The solid solute concentration during alloy solidification can be expressed by the following formula [44,45]:

$$C_S = k_0 C_L (1 - f_s)^{k_0 - 1} \quad (1)$$

k_0 is the equilibrium partition coefficient, which is defined as the ratio of the solute concentration in the solid-liquid two equilibrium phases at a certain temperature, namely C_S/C_L. C_S (wt.%) and C_L (wt.%) are the equilibrium concentrations of the solid and liquid phases, respectively. According to the Al-Cu binary phase diagram and existing research, the equilibrium partition coefficient of the Cu element is about 0.17 [46], which indicates that the content of Cu in the solid phase that solidifies preferentially is at a very low level.

The redistribution of solute atoms in molten metal during the solidification leads to the decrease of liquidus temperature at the front end of the solid-liquid interface, so the supercooling degree at a certain distance away from the solid-liquid interface is even greater than the front of the solid-liquid interface, which will result in the solidification interface develops from straight to dendritic. Finally, the remaining Cu-rich liquid phase solidifies between dendrites or dendrite arms to form the Cu-rich phase, resulting in strong segregation of Cu elements. Intergranular phases due to segregation will seriously affect

the performance of the joint during tensile testing [18]. As depicted in Figure 10b,d,f, the fracture mode of the 2A55 joint is mainly intergranular fracture, and a large number of intergranular phases appear on the fracture. The EDS results of these phases are recorded in Table 4.

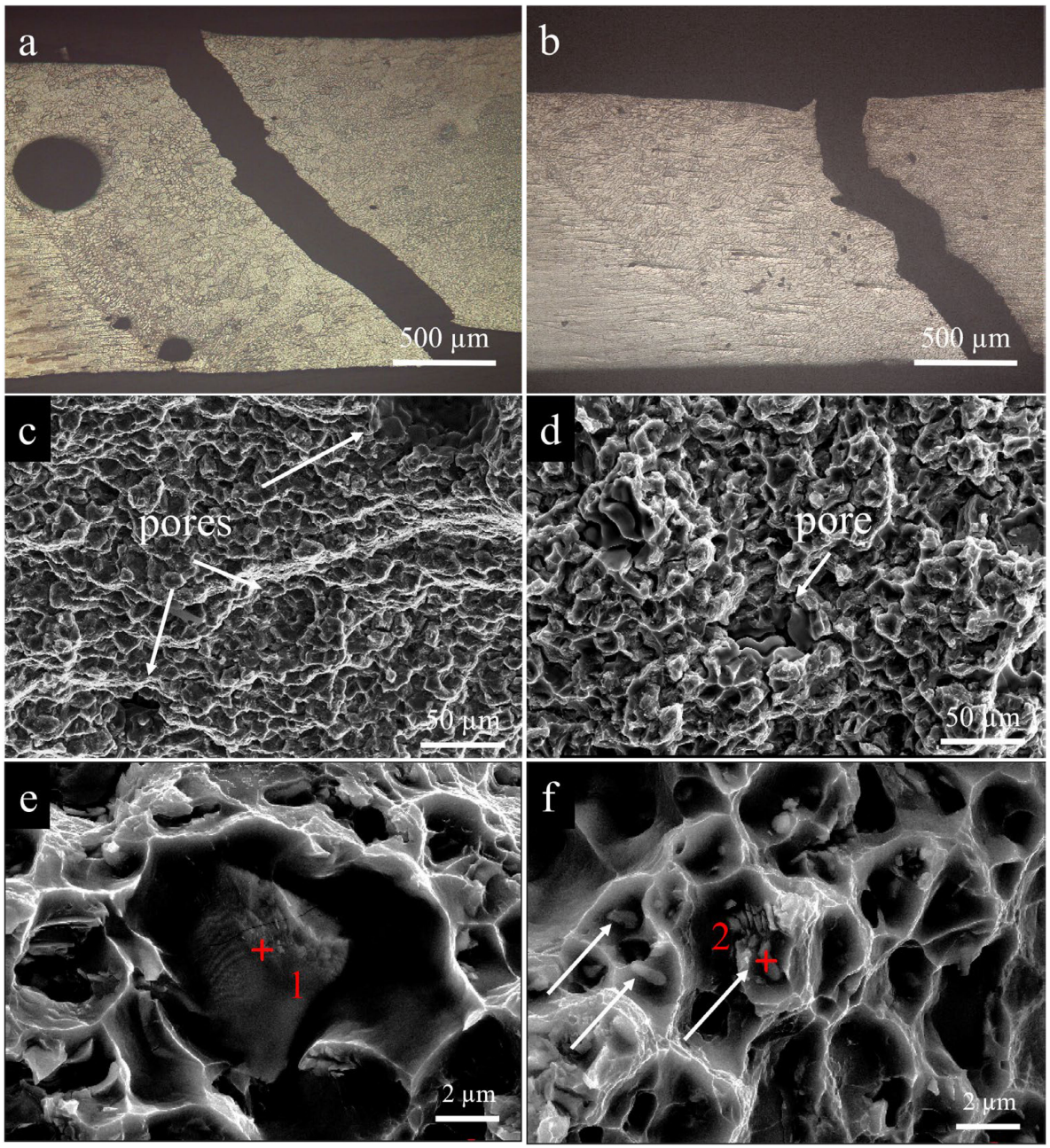

Figure 10. Cross-sectional metallography of fracture of (**a**) Al-8Cu, (**b**) 2A55 joint, SEM images of fracture of (**c**) Al-8Cu, (**d**) 2A55 joint, and EDS analysis position of (**e**) Al-8Cu, (**f**) 2A55 joint.

Table 4. EDS analysis results of marked position in Figure 10 (wt.%).

	Cu	Ti	Zr	Al
1	4.14	26.46	30.56	Bal.
2	19.97	/	2.53	Bal.

In addition, the addition of Ti and Zr elements is intended to refine the grains, improving the joint's performance by the grain refinement strengthening [36]. In the current work, Figure 2 can imply that when 0.3 wt.% Zr and Ti are co-added in the Al-8Cu filler wire. The grain size of the joint is much different from that using 2A55 filler wire containing 0.11 wt.% Zr and 0.06 wt.% Ti. During solidification, when the Zr and Ti content reaches the peritectic reaction component, the primary Al_3Zr or $TiAl_3$ particles can be precipitated in the melt [21,47]. As particles coherent with the matrix, these particles will act as heterogeneous nucleation particles to promote nucleation in the melt. According to the crystallization theory, the number of grains per unit area Z_s (cm^{-2}) can be expressed as the relationship between the nucleation rate N ($s^{-1}{\cdot}cm^{-3}$) and the grain growth rate V_g (cm/s):

$$Z_s = 1.1\left(N/V_g\right)^{1/2} \quad (2)$$

Under the condition of constant V_g, the increase of N leads to an increase in the number of grains per unit area, manifested as a decrease in grain size. However, as depicted in Figures 3a and 10e, a coarse phase containing Ti and Zr will appear in the Al-8Cu weld, which not only consumes a large amount of Ti and Zr but also reduces the ductility of the joint due to the coarse phase included in the grain boundary [18,48–50]. As indicated in Figure 10a,c, despite the presence of pores on the fusion line, the fracture occurred inside the weld, and coarse Ti and Zr phases were found on the fracture. Similar to the 2A55 joint, the fracture morphology of the Al-8Cu joint also shows intergranular fracture mode due to the effect of coarse intergranular phases.

4.2. Effect of Filler Wire on Precipitation Behavior of Joints

Previous microhardness and tensile tests showed that both the Al-8Cu joint and 2A55 joint exhibited poor strength and plasticity after one week of natural aging. Severe Cu segregation in the weld and the disappearance of the precipitates lead to this consequence.

The main strengthening precipitates of 2A55 alloy are $T_1(Al_2CuLi)$ and $\theta'(Al_2Cu)$ precipitation [5–7,47]. This work proves that the TIG welding process completely changes the type and number of precipitates in the weld. During the TIG welding process, the metal at the weld experienced melting and rapid solidification. At this time, many precipitates in the original BM have been dissolved, and the subsequent solidification process will only produce a small number of primary particles, such as Al_3Zr and Al_3Li, by the peritectic reaction.

Due to the fast solidification rate of the welding process, a large number of Li atoms are supersaturated solid solutions in the Al matrix of 2A55 weld. Subsequently, the supersaturation provides a driving force for the formation of fine and dispersed Al_3Li particles. Additionally, Li atoms can combine with Al_3Zr particles to form $Al_3(Zr, Li)$ composite particles [8,19,51]. However, the segregation during solidification consumes a large amount of Cu to form Cu-rich phases, resulting in low supersaturation of the solid solution, which cannot provide a sufficient driving force for subsequent precipitation. Therefore, except for a small number of GPZs, Cu-containing precipitates such as T_1, θ', and $S'(Al_2CuMg)$ are basically not precipitated during the natural aging process.

As for the Al-8Cu weld, even under the influence of element segregation, a part of the Cu atoms still remains in the Al matrix and slowly precipitates GPZs at room temperature. In addition to exploring the natural aging precipitation behavior of the welds, the DSC experiment also explored the evolution of the precipitates when the sample was heated. As shown in Figure 7 (Peak E), the Al-8Cu weld is slightly stronger than the 2A55 weld in the re-precipitation ability of Al_2Cu. The higher Cu content of the joint allows Al-8Cu to provide better thermal conditions for Al_2Cu precipitation under heating conditions. However, natural aging is carried out at room temperature, the diffusion rate of solid solution atoms is low, and the kinetic conditions for the formation of Al_2Cu are insufficient. Furthermore, as shown in Figure 8c, a few Al_3Li precipitates also appeared in the Al-8Cu weld. The Al-8Cu filler wire does not contain a Li element, even if part of the BM melts

into the weld, which leads to low Li content in the weld. The consequence is that there are not enough Li atoms dissolved in the Al matrix to provide thermal conditions for the precipitation of Al_3Li, and only a small number of Al_3Li particles are precipitated during natural aging.

5. Conclusions

1. When using the Al-8Cu welding wire designed for this work and 2A55 welding wire for TIG welding of 2A55 Al-Li alloy, the joints are well formed without obvious cracks and a small number of pores on the fusion line.
2. The joint addition of Zr and Ti contributed to the grain refinement of the weld. The equiaxed dendrite grain size in 2A55 weld (0.11 wt.% Zr + 0.1 Ti wt.%) and Al-8Cu weld (0.3 Zr wt.% + 0.3 Ti wt.%) is about 254 μm and 110 μm, respectively. However, coarse Zr and Ti phases were found in the Al-8Cu weld and fracture, acting as grain boundary inclusions, affecting the joint performance.
3. Strong segregation of Cu elements exists in TIG welded joints, which seriously reduces the plasticity of joints. In addition, the weld loses the dominant strengthening precipitation phase, and the number of precipitation phases is quite small, resulting in a great reduction in strength.
4. The obtained TIG welded joints can naturally precipitate Al_3Li particles or GPZs to strengthen welds. When the aging time was increased from one week to six months, the YS of the 2A55 joint increased by 24.1% compared to 14.7% for the Al-8Cu joint.

The natural aging strengthening behavior of the 2A55 Al-Li alloy TIG joint was studied in this work. However, the performance of the joints can be further improved by performing appropriate pre-and post-treatment. For example, preheating the substrate before welding can reduce the weld's solidification rate and the sensitivity of hot cracking. At the same time, the gas in the molten pool can be allowed to escape. In addition, appropriate mechanical-based post-treatment, such as rolling and peening, can modify the surface of the joint to eliminate residual stress and improve the fatigue performance and corrosion resistance of the joints.

Author Contributions: Conceptualization, J.L.; methodology, J.L. and R.Z.; literature search, Z.L., P.L. and R.Z.; study design, Z.L., P.L., H.X. and Y.H.; investigation, Z.L., H.X. and Y.H.; resources, P.L., P.M. and Y.C.; data curation, Z.L.; writing—original draft preparation, Z.L.; writing—review and editing, R.Z. and J.L. All authors have read and agreed to the published version of the manuscript.

Funding: This work is supported by the Natural Science Foundation of Hunan Province (2021JJ40773).

Data Availability Statement: The data presented in this study are available on request from the corresponding author. The data are not publicly available.

Acknowledgments: The authors thank G. Zeng for his assistance with the DSC tests.

Conflicts of Interest: The authors declare no conflict of interest.

References

1. Eddahbi, M.; Thomson, C.; Carreño, F.; Ruano, O. Grain structure and microtexture after high temperature deformation of an Al–Li (8090) alloy. *Mater. Sci. Eng. A* **2000**, *284*, 292–300. [CrossRef]
2. Yoshimura, R.; Konno, T.; Abe, E.; Hiraga, K. Transmission electron microscopy study of the evolution of precipitates in aged Al–Li–Cu alloys: The θ′ and T1 phases. *Acta Mater.* **2003**, *51*, 4251–4266. [CrossRef]
3. Rioja, R.J.; Liu, J. The Evolution of Al-Li Base Products for Aerospace and Space Applications. *Metall. Mater. Trans. A Phys. Metall. Mater. Sci.* **2012**, *43*, 3325–3337. [CrossRef]
4. Dursun, T.; Soutis, C. Recent developments in advanced aircraft aluminium alloys. *Mater. Des.* **2014**, *56*, 862–871. [CrossRef]
5. Li, J.; Liu, P.; Chen, Y.; Zhang, X.; Zheng, Z. Microstructure and mechanical properties of Mg, Ag and Zn multi-microalloyed Al–(3.2–3.8)Cu–(1.0–1.4)Li alloys. *Trans. Nonferrous Met. Soc. China* **2015**, *25*, 2103–2112. [CrossRef]
6. Liu, Q.; Zhu, R.; Li, J.; Chen, Y.; Zhang, X.; Zhang, L.; Zheng, Z. Microstructural evolution of Mg, Ag and Zn micro-alloyed Al–Cu–Li alloy during homogenization. *Trans. Nonferrous Met. Soc. China* **2016**, *26*, 607–619. [CrossRef]

7. Lu, D.-D.; Wang, G.; Li, J.-F.; Deng, S.-X.; Huang, Y.; Xiang, H.; Yao, Y.; Ma, P.-C.; Chen, Y.-L.; Zhang, X.-H. Effect of grain structure and precipitate on tensile properties and low-cycle fatigue behaviors of 2A55 Al-Cu-Li alloy. *Int. J. Fatigue* **2022**, *159*, 106834. [CrossRef]
8. Fu, B.; Qin, G.; Meng, X.; Ji, Y.; Zou, Y.; Lei, Z. Microstructure and mechanical properties of newly developed aluminum–lithium alloy 2A97 welded by fiber laser. *Mater. Sci. Eng. A* **2014**, *617*, 1–11. [CrossRef]
9. Ding, J.-K.; Wang, D.-P.; Wang, Y.; DU, H. Effect of post weld heat treatment on properties of variable polarity TIG welded AA2219 aluminium alloy joints. *Trans. Nonferrous Met. Soc. China* **2014**, *24*, 1307–1316. [CrossRef]
10. Wan, Z.; Wang, Q.; Zhao, Y.; Zhao, T.; Shan, J.; Meng, D.; Song, J.; Wu, A.; Wang, G. Improvement in tensile properties of 2219-T8 aluminum alloy TIG welding joint by PMZ local properties and stress distribution. *Mater. Sci. Eng. A* **2022**, *839*, 142863. [CrossRef]
11. Li, H.; Zou, J.; Yao, J.; Peng, H. The effect of TIG welding techniques on microstructure, properties and porosity of the welded joint of 2219 aluminum alloy. *J. Alloy. Compd.* **2017**, *727*, 531–539. [CrossRef]
12. Li, Q.; Wu, A.-P.; Li, Y.-J.; Wang, G.-Q.; Qi, B.-J.; Yan, D.-Y.; Xiong, L.-Y. Segregation in fusion weld of 2219 aluminum alloy and its influence on mechanical properties of weld. *Trans. Nonferrous Met. Soc. China* **2017**, *27*, 258–271. [CrossRef]
13. Samiuddin, M.; Li, J.-L.; Taimoor, M.; Siddiqui, M.N.; Siddiqui, S.U.; Xiong, J.-T. Investigation on the process parameters of TIG-welded aluminum alloy through mechanical and microstructural characterization. *Def. Technol.* **2020**, *17*, 1234–1248. [CrossRef]
14. Zhang, D.-K.; Wu, A.-P.; Zhao, Y.; Shan, J.-G.; Wan, Z.-D.; Wang, G.-Q.; Song, J.-L.; Zhang, Z.-P.; Liu, X.-L. Microstructural evolution and its effect on mechanical properties in different regions of 2219-C10S aluminum alloy TIG-welded joint. *Trans. Nonferrous Met. Soc. China* **2020**, *30*, 2625–2638. [CrossRef]
15. Chen, Q.; Ge, H.; Yang, C.; Lin, S.; Fan, C. Study on Pores in Ultrasonic-Assisted TIG Weld of Aluminum Alloy. *Metals* **2017**, *7*, 53. [CrossRef]
16. Faraji, A.H.; Moradi, M.; Goodarzi, M.; Colucci, P.; Maletta, C. An investigation on capability of hybrid Nd:YAG laser-TIG welding technology for AA2198 Al-Li alloy. *Opt. Lasers Eng.* **2017**, *96*, 1–6. [CrossRef]
17. Zhang, Y.; Li, H.; Luo, C.; Yang, L. Effects of Filler Wires on the Microstructure and Mechanical Properties of 2195-T6 Al-Li Alloy Spray Formed by TIG Welding. *Materials* **2019**, *12*, 3559. [CrossRef]
18. Solórzano, I.; Darwish, F.; de Macedo, M.; de Menezes, S. Effect of weld metal microstructure on the monotonic and cyclic mechanical behavior of tig welded 2091 Al–Li alloy joints. *Mater. Sci. Eng. A* **2003**, *348*, 251–261. [CrossRef]
19. Kostrivas, A.D.; Lippold, J.C. Simulating weld-fusion boundary microstructures in aluminum alloys. *Jom* **2004**, *56*, 65–72. [CrossRef]
20. Wang, B.; Xue, S.-B.; Ma, C.-L.; Han, Y.-L.; Lin, Z.-Q. Effect of combinative addition of Ti and Sr on modification of AA4043 welding wire and mechanical properties of AA6082 welded by TIG welding. *Trans. Nonferrous Met. Soc. China* **2017**, *27*, 272–281. [CrossRef]
21. Zeren, M.; Karakulak, E. Influence of Ti addition on the microstructure and hardness properties of near-eutectic Al–Si alloys. *J. Alloy. Compd.* **2008**, *450*, 255–259. [CrossRef]
22. Kinner-Becker, T.; Hettig, M.; Sölter, J.; Meyer, D. Analysis of internal material loads and Process Signature Components in deep rolling. *CIRP J. Manuf. Sci. Technol.* **2021**, *35*, 400–409. [CrossRef]
23. Nie, L.; Wu, Y.; Gong, H.; Chen, D.; Guo, X. Effect of Shot Peening on Redistribution of Residual Stress Field in Friction Stir Welding of 2219 Aluminum Alloy. *Materials* **2020**, *13*, 3169. [CrossRef] [PubMed]
24. Toursangsaraki, M.; Hu, Y. Crystal plasticity evaluation of laser peening effects on improving high-cycle fatigue life of Al-Li friction stir welded joints. *Mater. Des.* **2022**, *223*, 111147. [CrossRef]
25. Zhao, T.; Sato, Y.S.; Xiao, R.; Huang, T.; Zhang, J. Hardness distribution and aging response associated with precipitation behavior in a laser pressure welded Al–Li alloy 2198. *Mater. Sci. Eng. A* **2021**, *808*, 140946. [CrossRef]
26. Yi, J.; Wang, G.; Li, S.-K.; Liu, Z.-W.; Gong, Y.-L. Effect of post-weld heat treatment on microstructure and mechanical properties of welded joints of 6061-T6 aluminum alloy. *Trans. Nonferrous Met. Soc. China* **2019**, *29*, 2035–2046. [CrossRef]
27. Kumar, K.; Heubaum, F. The effect of Li content on the natural aging response of Al_Cu_Li_Mg_Ag_Zr alloys. *Acta Mater.* **1997**, *45*, 2317–2327. [CrossRef]
28. Ivanov, R.; Deschamps, A.; De Geuser, F. Clustering kinetics during natural ageing of Al-Cu based alloys with (Mg, Li) additions. *Acta Mater.* **2018**, *157*, 186–195. [CrossRef]
29. Ivanov, R.; Deschamps, A.; De Geuser, F. High throughput evaluation of the effect of Mg concentration on natural ageing of Al-Cu-Li-(Mg) alloys. *Scr. Mater.* **2018**, *150*, 156–159. [CrossRef]
30. Jambora, F.M.; Bokůvkaa, O.; Trškob, L. The natural aging behavior of the AA 2055 Al-Cu-Li alloy. *Transp. Res. Procedia* **2019**, *40*, 42–45. [CrossRef]
31. Dong, J.S.; Yang, D.; Cui, Y.; Jiang, L. Age-hardening behavior of a SiCw/Al-Li-Cu-Mg-Zr composite. *Mater. Sci. Eng. A* **2002**, *327*, 213–223. [CrossRef]
32. Wu, C.; Li, H.; Bian, T.; Lei, C.; Zhang, L. Natural aging behaviors of Al-Cu-Li alloy: PLC effect, properties and microstructure evolution. *Mater. Charact.* **2022**, *184*, 111694. [CrossRef]
33. Wu, L.; Chen, Y.; Li, X.; Ma, N.; Wang, H. Rapid hardening during natural aging of Al-Cu-Li based alloys with Mg addition. *Mater. Sci. Eng. A* **2018**, *743*, 741–744. [CrossRef]

34. Manikandan, P.; Chakravadhanula, V.; Rao, G.S.; Manwatkar, S.K.; Murty, S.N.; Sivakumar, D.; Pant, B.; Mohan, M. Effect of long-term natural aging on the tensile and fracture properties of aluminum alloy AA2219-T87 parent and weldments at room and cryogenic temperatures. *Mater. Charact.* **2022**, *189*, 111973. [CrossRef]
35. Zhong, S.; Han, S.; Chen, J.; Ren, J.; Zhou, Z.; Wen, F.; Qi, L.; Guan, R. Microstructure and properties of 7075 aluminum alloy welding joint using different filler metals. *Mater. Today Commun.* **2022**, *31*, 103260. [CrossRef]
36. Yuan, Z.-S.; Lu, Z.; Xie, Y.-H.; Dai, S.-L.; Liu, C.-S. Effects of RRA Treatments on Microstructures and Properties of a New High-strength Aluminum-Lithium Alloy-2A97. *Chin. J. Aeronaut.* **2007**, *20*, 187–192. [CrossRef]
37. Dorin, T.; Deschamps, A.; De Geuser, F.; Lefebvre, W.; Sigli, C. Quantitative description of the T1 formation kinetics in an Al–Cu–Li alloy using differential scanning calorimetry, small-angle X-ray scattering and transmission electron microscopy. *Philos. Mag.* **2014**, *94*, 1012–1030. [CrossRef]
38. Martin, J.H.; Yahata, B.D.; Hundley, J.M.; Mayer, J.A.; Schaedler, T.A.; Pollock, T.M. 3D printing of high-strength aluminium alloys. *Nature* **2017**, *549*, 365–369. [CrossRef]
39. Kim, H.T.; Nam, S.W. Solidification cracking susceptibility of high strength aluminum alloy weldment. *Scr. Mater.* **1996**, *34*, 1139–1145. [CrossRef]
40. Li, L.; Li, R.; Yuan, T.; Chen, C.; Zhang, Z.; Li, X. Microstructures and tensile properties of a selective laser melted Al–Zn–Mg–Cu (Al7075) alloy by Si and Zr microalloying. *Mater. Sci. Eng. A* **2020**, *787*, 139492. [CrossRef]
41. Wang, J.; Liu, Z.; Bai, S.; Cao, J.; Zhao, J.; Luo, L.; Li, J. Microstructure evolution and mechanical properties of the electron-beam welded joints of cast Al–Cu–Mg–Ag alloy. *Mater. Sci. Eng. A* **2021**, *801*, 140363. [CrossRef]
42. Coniglio, N.; Cross, C.E. Initiation and growth mechanisms for weld solidification cracking. *Int. Mater. Rev.* **2013**, *58*, 375–397. [CrossRef]
43. Rappaz, M.; Jacot, A.; Boettinger, W.J. Last-stage solidification of alloys: Theoretical model of dendrite-arm and grain coalescence. *Met. Mater. Trans. A* **2003**, *34*, 467–479. [CrossRef]
44. Guo, Y.-J.; Li, J.-F.; Lu, D.-D.; Deng, S.-X.; Zeng, G.-J.; Ma, Y.-L.; You, W.; Chen, Y.-L.; Zhang, X.-H.; Zhang, R.-F. Characterization of Al3Zr precipitation via double-step homogenization and recrystallization behavior after subsequent deformation in 2195 Al-Li alloy. *Mater. Charact.* **2021**, *182*, 111549. [CrossRef]
45. Pu, Q.Q.; Jia, Z.H.; Kong, Y.P.; Yang, Q.B.; Zhang, Z.Q.; Fan, X.; Zhang, H.; Lin, L.; Liu, Q. Microstructure and mechanical properties of 2195 alloys prepared by traditional casting and spray forming. *Mater. Sci. Eng. A* **2020**, *784*, 139337. [CrossRef]
46. Gao, Z.; Liu, J.; Chen, J.; Duan, S.; Liu, Z.; Ming, W.; Wu, C. Formation mechanism of precipitate T1 in AlCuLi alloys. *J. Alloy. Compd.* **2014**, *624*, 22–26. [CrossRef]
47. Zeng, G.-J.; Ning, H.; Deng, S.-X.; Li, J.-F.; Yao, Y.; Guo, Y.-J.; Lu, D.-D.; Li, Y.-Z.; Liu, Z.-H.; Ma, P.-C.; et al. Quantification of the Effect of Increased Pre-Deformation on Microstructure and Mechanical Properties of 2A55 Al–Li Alloy. *Adv. Eng. Mater.* **2022**, *24*, 2200033. [CrossRef]
48. Liu, J.; Zhang, K.; Yang, Y.; Wang, H.; Zhu, Y.; Huang, A. Grain boundary α-phase precipitation and coarsening: Comparing laser powder bed fusion with as-cast Ti-6Al-4V. *Scr. Mater.* **2021**, *207*, 114261. [CrossRef]
49. Tian, X.; Zhu, Y.; Lim, C.V.S.; Williams, J.; Boyer, R.; Wu, X.; Zhang, K.; Huang, A. Isotropic and improved tensile properties of Ti-6Al-4V achieved by in-situ rolling in direct energy deposition. *Addit. Manuf.* **2021**, *46*, 102151. [CrossRef]
50. Zhang, R.; Li, J.; Li, Q.; Qi, Y.; Zeng, Z.; Qiu, Y.; Chen, X.; Kairy, S.; Thomas, S.; Birbilis, N. Analysing the degree of sensitisation in 5xxx series aluminium alloys using artificial neural networks: A tool for alloy design. *Corros. Sci.* **2019**, *150*, 268–278. [CrossRef]
51. Yang, D.; Li, X.; He, D.; Huang, H. Effect of minor Er and Zr on microstructure and mechanical properties of Al–Mg–Mn alloy (5083) welded joints. *Mater. Sci. Eng. A* **2013**, *561*, 226–231.